



HAL
open science

Plastic behavior-dependent weldability of heat-treatable aluminum alloys in friction stir welding

Danilo Ambrosio, Vincent Wagner, Gilles Dessenin, Jean-Yves Paris, KhouLOUD Jlaiel, Olivier Cahuc

► **To cite this version:**

Danilo Ambrosio, Vincent Wagner, Gilles Dessenin, Jean-Yves Paris, KhouLOUD Jlaiel, et al.. Plastic behavior-dependent weldability of heat-treatable aluminum alloys in friction stir welding. *International Journal of Advanced Manufacturing Technology*, 2021, 117 (1-2), pp.635-652. 10.1007/s00170-021-07754-4 . hal-03479406

HAL Id: hal-03479406

<https://hal.science/hal-03479406v1>

Submitted on 2 Oct 2024

HAL is a multi-disciplinary open access archive for the deposit and dissemination of scientific research documents, whether they are published or not. The documents may come from teaching and research institutions in France or abroad, or from public or private research centers.

L'archive ouverte pluridisciplinaire **HAL**, est destinée au dépôt et à la diffusion de documents scientifiques de niveau recherche, publiés ou non, émanant des établissements d'enseignement et de recherche français ou étrangers, des laboratoires publics ou privés.

Plastic behavior-dependent weldability of heat-treatable aluminum alloys in friction stir welding

Danilo Ambrosio · Vincent Wagner ·
Gilles Dessein · Jean-Yves Paris ·
Khouloud Jlaiel · Olivier Cahuc

Received: date / Accepted: date

Abstract The quality of friction stir welding joints is intimately related to the correct mixing of the stirred material. The material flow is strongly dependent on the plastic behavior of the welded alloy. For this reason, the friction stir weldability depends on the structure, microstructure and chemical composition of the base material. In this work, in-plane forces and acoustic emission signals were monitored while welding two heat-treatable aluminum alloys. The forces evolutions suggested possible continuous and intermittent material flow during friction stir welding depending on the welding parameters. The differences observed in the in-plane forces were corroborated by acoustic emission, confirming the modification in the material flow phenomenology. Therefore, differences observed in aluminum alloys' friction stir weldability are due to the plastic behavior at high temperature and medium-high strain rate. The higher the deformability of the aluminum alloys, the wider the weldability window in friction stir welding because of continuous material flow in an extended range of process parameters.

Keywords Friction stir welding · Forces · Acoustic emission · Plastic behavior · Material flow

1 Introduction

The revolutionary solid-state welding process known as friction stir welding (FSW) was invented in 1991 [1]. Since then, it has been the focus of countless research to understand the complex mechanisms of this welding technique to increase its use in industry. Among the several investigations on different materials, the friction stir welding of aluminum alloys (AA) 6xxx and 7xxx families has been widely studied for their relevance for the automotive [2] and aerospace [3] industries. The

D. Ambrosio (dambrosi@enit.fr) · V. Wagner · G. Dessein · J.-Y. Paris · K. Jlaiel
Laboratoire Génie de Production, ENI Tarbes, 65016 Tarbes, France
O. Cahuc
University of Bordeaux, Institute of mechanics and engineering (I2M), CNRS, 33400 Talence, France

extrapolation of all the results obtained in the various studies is complicated because of the high number of variables such as process parameters, type of control (force or position), tool geometry, etc. However, a rough weldability window can be identified by gathering the literature results on sheets thickness equal to or below 6 mm and considering only welding and rotational speed. The percentage of sound weld out of all the trials found in literature can be an indicator of the specific alloy's weldability. By sound weld is meant a joint that has neither internal nor external defects. From the analysis of the work provided on AA6xxx-T6 [4, 5, 6, 7, 8] and AA7075-T6 [9, 10, 11, 12, 13, 14, 15, 16], it was evident the greater weldability of the former, as shown in Fig. 1. Specifically, it is interesting to observe

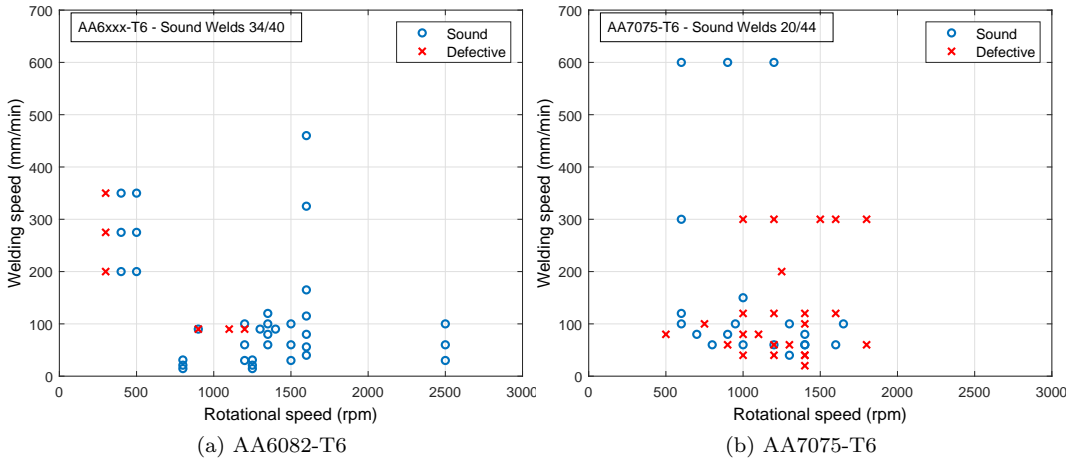


Fig. 1 Weldability windows for AA6xxx-T6 and AA7075-T6 from previous works.

the high defectiveness at a rotational speed equal to or higher than 1000 rpm for AA7075-T6. These results demonstrate different weldability of the materials, even though they are two aluminum alloys.

The only study found focusing on the weldability of aluminum alloys to explain their different plastic behavior was proposed by Leitão et al. [5] in their analysis of AA5083-H11 and AA6082-T6 friction stir weldability. The authors justified the different weldability windows by the plastic behavior of the materials at high temperatures, relying on quasi-static mechanical characterization tests at temperatures similar to those reached during the FSW process. The good weldability of AA6082-T6 was attributed to its sensitivity to the intense flow softening in FSW conditions.

Although not straightforward due to the impossibility of accessing the deformed zone during the process, the investigation of the plastic behavior of aluminum alloys in friction stir welding is fundamental for the real understanding of the process. An alternative approach based on the measurement of physical quantities intrinsically connected to the tool-workpiece interaction is proposed. In this case, it refers to the in-plane forces and acoustic emission signals generated during the process. The evolution of in-plane forces during friction stir welding has been

extensively studied over the last twenty years. The information in these studies confirmed the changes in the plastic behavior of welded materials as the process parameters change. Specifically, the welding force decreases with rotational speed until a minimum is reached and then slightly increases again if rotation continues to be increased [17]. On the contrary, by increasing the welding speed, the welding force increases due to the less time available for the heat to diffuse and soften the material [18]. Furthermore, as far as the occurrence of defects is concerned, it has been suggested the correlation between defective joints and irregular evolution of in-plane forces [19,20]. Hence, a correlation between anomalies in the oscillatory nature of the in-plane forces and defects has been demonstrated [21]. Contrarily, acoustic emission (AE) technique has been rarely employed for monitoring friction stir welding. Very few studies were proposed to detect the occurrence of defects [22], to study the evolution of AE signals with welding parameters [23] and recently, a model was developed to assess the quality and strength of friction stir welds employing AE signals together with machine vision [24].

The authors propose an alternative investigation of plastic behavior by monitoring forces and acoustic emission signals while welding two different aluminum alloys, AA6082-T6 and AA7075-T6. Identical welding conditions were tested on both alloys to see any plastic behavior differences under the same welding conditions. The objective is to find differences in the monitored quantities due to the plastic behavior of the two materials and explain the different weldability windows. The results may elucidate differences in weldability windows according to the considered aluminum alloys' plastic behavior.

2 Methods

2.1 Experimental devices

The tests were performed on an adapted CNC lathe machine, Somab Genymab 900. The welding forces were recorded using a Kistler quartz three-component dynamometer type 9255C. The acquisition was carried out with Dynaware software at 1500 Hz. The in-plane forces can be separated into two components: F_x and F_y which are, respectively, the component in the welding direction (i.e., welding force) and the transversal one (i.e., transversal force).

Acoustic emission acquisitions were performed using two sensors fixed on two corners on the same side of the support system, as displayed in Fig. 2. As the sensors gave similar signals, only the signals from the one closer to the plunging point were considered in this article. A large band sensor type operating whose maximum sensitivity ranged between 100 and 1000 kHz was employed. The sensor was set using a water-based adhesive containing styrene acrylic copolymer. Through trial tests, the threshold value of 30 dB was chosen to remove possible noise due to the environment rather than process-related phenomena. The sample rate was set at 1 MSPS (Mega Samples Per Second), and an amplifier operating with a single-ended was set at 40 dB.

The internal quality of the joints was inspected through the use of an optical microscope (Olympus PMG3) after properly polishing the specimens and etching them with Kellers reagent. The samples were all taken at the same position, 10 mm before the exit point, to make sure they were in the steady-state of the process.

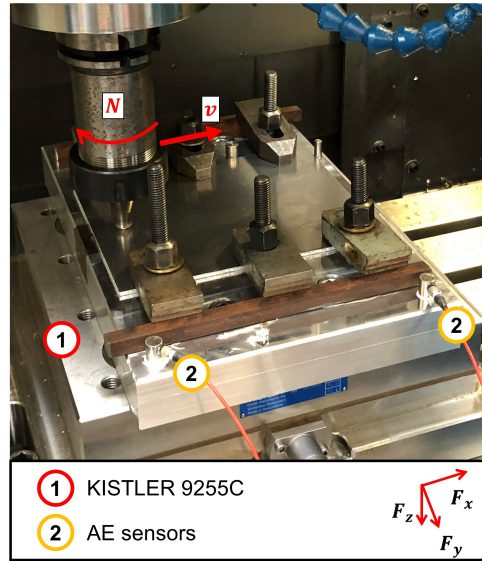


Fig. 2 Experimental setup. Three-axis loadcell and acoustic emission sensors.

2.2 Friction stir tools and materials

Four different combinations of process parameters were tested per material, as displayed in Tab. 1. The welding speed was kept constant at 180 mm/min. The 70

Table 1 Process parameters in the tested configuration. Rotational speed (N), welding speed (v), advance per revolution (APR), plunge depth (d).

Material	N (rpm)	APR (mm/rev)	d (mm)
AA6082-T6	750	0.24	0.3
	1000	0.18	0.25
	1500	0.12	0.25
	2000	0.09	0.2
AA7075-T6	500	0.36	0.3
	1000	0.18	0.25
	1500	0.12	0.25
	2000	0.09	0.2

mm long bead-on-plates were carried out on 3 mm thick sheets along the rolling direction for AA7075-T6 and perpendicularly to it for AA6082-T6. Some mechanical and thermal properties of the two materials are shown in Tab. 2. It is also worth reporting some information regarding the chemical composition of

Table 2 Mechanical and thermal properties of AA6082-T6 and AA7075-T6. Yield stress (Y), ultimate tensile strength (UTS), solidus temperature ($T_{solidus}$), specific heat (c), thermal conductivity (λ) [25]

Material	Y (MPa)	UTS (MPa)	$T_{solidus}$ (°C)	c (J/kgK)	λ (W/mK)
AA6082-T6	270	330	580	900	160
AA7075-T6	503	572	477	960	130

the two alloys. AA6082-T6 is made of aluminum between 95-98%, and the highest percentages of alloying agents are silicon, magnesium, and manganese. Contrarily, in AA7075-T6, the percentage of aluminum is between 87-92%, and the major alloying elements are zinc (5.6-6.1%), magnesium (2-2.5%), and copper (1.2-1.6%) [25].

The tool, manufactured by Stirweld out of H13 steel, was characterized by an 11,5 mm grooved shoulder diameter and frustum shape threaded pin with an upper and lower diameter of 5 and 4 mm, respectively. Mild steel was used as a backing plate.

2.3 Forces analysis

In-plane forces in FSW represent the resistance offered by the material during the tool rotation and advancing along the welding line. The material resistance depends on both thermal and mechanical aspects. During deformation, the higher the temperature, the stronger the thermal softening, and the decrease in the material strength [26]. The higher the strain rate, the higher the resistance offered by the material [27].

The analysis focuses on two factors, the in-plane force average values evolution as the rotational speed increases and the periodicity of these signals in the various tests to detect specific changes attributable to a perturbation of the process. The former can provide information regarding the overall resistance offered by the material to tool movement. It can therefore reveal whether the maximum softening has been achieved or not. The analysis of the harmonic part with a focus on single rotations can instead reveal disturbances attributable to instabilities that may occur during the cyclic pin-layer interaction.

2.4 Temperature measurement

The temperature measurement in the stirred zone was obtained through a thermal FEM model. A surface heat flux was applied on the shoulder-workpiece and lateral pin-workpiece contact areas, as shown in Fig. 3. To quantify the heat flux to be applied on the surfaces, the power generated during the process and the contact surfaces must be calculated. The mechanical power is attributable to the tool rotation and feed:

$$P = P_{rot} + P_{adv} = M\omega + F_x v \quad (1)$$

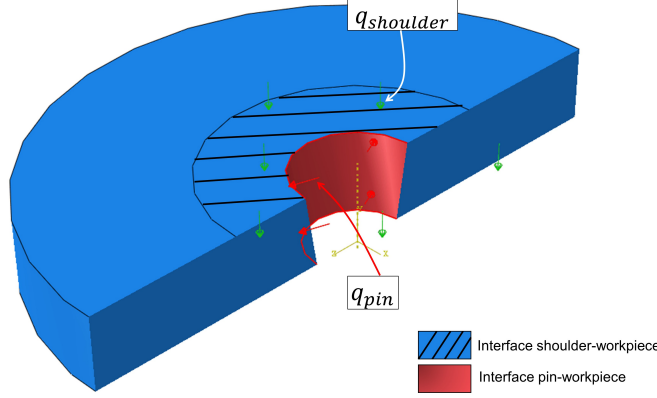


Fig. 3 180° view of the workpiece and the surface heat flux applied on the contact surfaces.

The rotary part is derived from the CNC machine's power output, while the advancing amount is calculated from the average force in the welding direction and the feed rate. Only part of this energy is converted into heat:

$$P_{heat} = \eta P \quad (2)$$

The η parameter represents the fraction of power transformed into heat. Based on previous work [28,29] this percentage has always been considered to be between 0.8 and 0.9. In this work, the parameter was used to calibrate simulation and fit experimental measurements. Then, the total heat flux must be split between the tool surfaces. For the sake of simplicity, features such as grooves and threads have not been considered. The contribution of the individual surfaces to the total heat generated can be determined using the Schmidt approach based on simple geometric considerations [30]:

$$f_s = \frac{A_{shoulder}}{A_{shoulder} + A_{pin}} = 0.67 \quad (3)$$

$$f_p = \frac{A_{pin}}{A_{shoulder} + A_{pin}} = 0.33 \quad (4)$$

The parameter f represents the heat generation ratio from the considered surface. Therefore, it is possible to obtain the surface heat flux by dividing the heat generated by the shoulder and pin by their surfaces:

$$q_{shoulder} = \frac{f_s P_{heat}}{A_{shoulder}} \left[\frac{W}{m^2} \right] \quad (5)$$

$$q_{pin} = \frac{f_p P_{heat}}{A_{pin}} \left[\frac{W}{m^2} \right] \quad (6)$$

The bottom surface of the pin was neglected for simplicity as it represents less than 5% of the tool surface in contact with the material, and thus its low contribution to overall heat generation.

Regarding the boundary conditions, two different contact conditions were applied on the lower surface, contact with a steel backing plate, and the upper surface, contact with air. The convective heat transfer coefficient for the air is set at $15 \text{ W m}^{-2} \text{ K}^{-1}$ with an ambient temperature of $23 \text{ }^\circ\text{C}$. The interaction with the steel backing plate, fundamental to take into account the heat dissipation through this element has been introduced for simplicity through a convective heat transfer coefficient of $500 \text{ W m}^{-2} \text{ K}^{-1}$ [31].

The calibration of η was made fitting the experimental measurements found in the bibliography [32], with the experiments performed on AA6082-T6. The material employed in [32] was 4.5 mm AA6061 sheets, and the welding speed is 200 mm/min. The similarities between the materials, thicknesses, and roughly the same welding parameters allowed these data's employment for the model calibration. Experimental measurements were obtained with a thermocouple embedded in the tool shoulder very close to the pin. The η parameter has been fixed between 0.85 and 0.87, decreasing it from 500 to 2000 rpm taking into account the increase in heat losses increasing the heat generation. The comparison between the simulation results and the experimental measurements is shown in Fig. 4a. The $T_{max,NZ}$ obtained from the simulations is the highest around the tool, as displayed in Fig.4b. The differences between experiments and simulations are lower than 5%

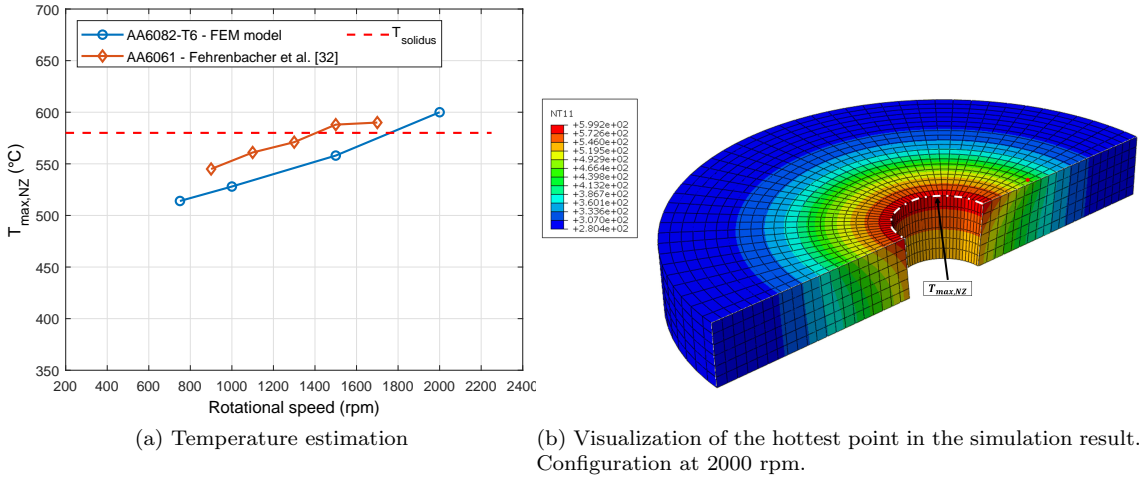


Fig. 4 Comparison with temperature measurement in bibliography.

confirming the FEM thermal model's reliability for predicting the maximum temperature during welding. Moreover, since a 15 mm shoulder diameter was used by Fehrenbacher et al. [32] while in the test performed in this work on AA6082-T6, it is 11.5 mm, the difference between the real peak temperatures is further reduced.

3 Results

3.1 In-plane forces

The average in-plane forces evolution with rotational speed for both aluminum alloys is shown in Fig. 5.

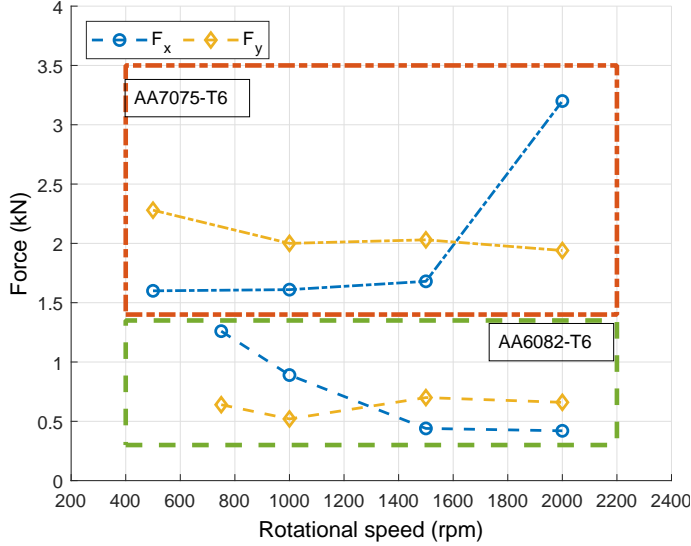


Fig. 5 Average value of in-plane forces as a function of the rotational speed.

For AA6082-T6, the force in the welding direction decreases by 65% between 750 and 1500 rpm and then stabilizes between 1500 and 2000 rpm when likely the max softening is reached. The transversal component is constant in the whole investigated window of rotational speed with minimal differences. Also, for 750 and 1000 rpm $F_x > F_y$ while for 1500 and 2000 rpm $F_x < F_y$.

Regarding AA7075-T6, the welding force increases by 5% from 500 to 1500 rpm while it suddenly increases, almost doubling for a rotation of 2000 rpm. Conversely, the y component decreases by 12% between 500 and 1000 rpm and then stabilizes. About the relationship between the two components, the x component is greater than the y component over the entire range except for the 2000 rpm configuration. From these results, the different evolution of the in-plane forces for the two materials is highlighted. Specifically, AA7075-T6 showed stability in the range 500-1500 rpm, while AA6082-T6 displayed a substantial decrease between 750 and 1500 rpm of the welding force. The almost negligible influence of rotational speed on the transverse component is evident from tests on both aluminum alloys. Furthermore, it is noteworthy how the relationship between x and y components varies as the rotational speed varies and the overall higher value of forces reported for 7075-T6 alloy compared to 6082-T6.

3.2 Periodicity of in-plane forces

The periodic evolution of the in-plane forces during ten rotations is displayed in Fig. 6 and Fig. 7 for AA6082-T6 and AA7075-T6, respectively.

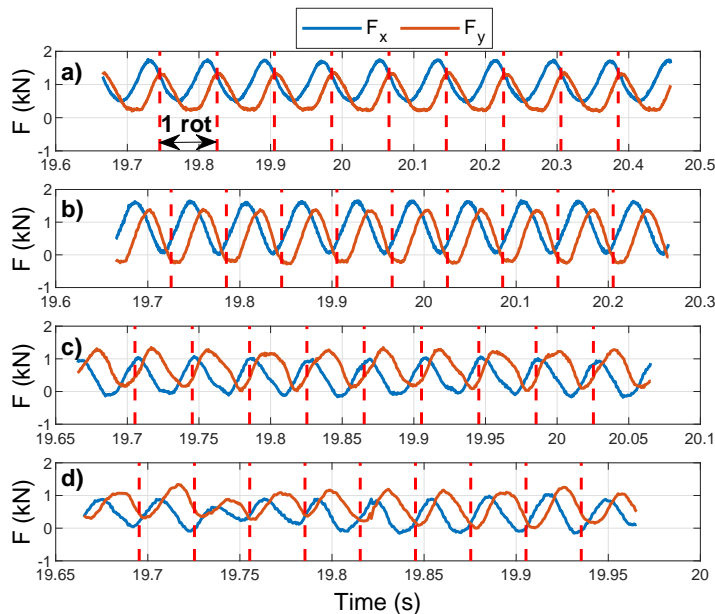


Fig. 6 Periodic evolution of in-plane forces over ten rotations while welding AA6082-T6. a) 750 rpm, b) 1000 rpm, c) 1500 rpm, d) 2000 rpm.

The dashed vertical red lines mark the period of one rotation in the various configurations. The evolution of the forces is stable for all the tested rotational speed welding AA6082-T6 with a periodicity coincident with the tool rotation (Fig. 6). It is possible to recognize the tool rotation with one peak and one valley in all the configurations. In contrast, the results for the tests performed on AA7075-T6 seem to belong to three groups. The first one is formed only by the configuration at 500 rpm (Fig. 7a) with the forces period equal to the tool's rotation and with a steady evolution of both forces around their average value. It is interesting to point out the momentary interruption in the growth of both forces before the peak is reached. The second group consists of the 1000 and 1500 rpm configurations, Fig. 7b and c, respectively. In some cases, it seems more peaks and valleys can be identified in one cycle, while in others, it is not even possible to find a peak and a valley. Strong instability characterizes these two intermediate configurations. Finally, in the 2000 rpm configuration (Fig. 7d), it is possible to find the periodicity equal to the tool rotation again but with an unexpected marked difference between the two forces.

The evolution of the in-plane forces revealed differences associated with the tool-workpiece interaction depending on the considered aluminum alloy. In all tested configurations, the in-plane forces developed during friction stir welding of AA6082-

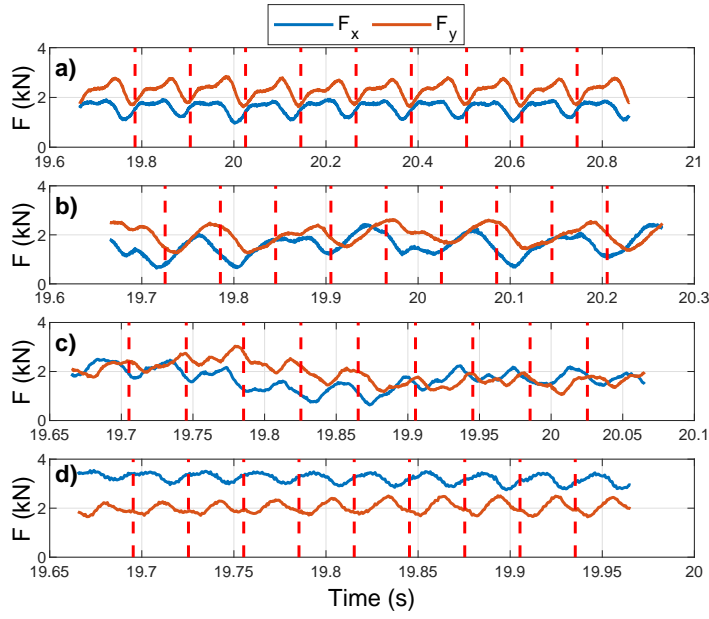


Fig. 7 Periodic evolution of in-plane forces over ten rotations while welding AA7075-T6. a) 500 rpm, b) 1000 rpm, c) 1500 rpm, d) 2000 rpm.

T6 showed a stable evolution around the average value with regular periodicity, i.e., one tool rotation, one peak and one valley with a perfect sinusoidal trend. Contrarily, the complexity of the mechanisms occurring during friction stir welding of AA7075-T6 has been captured by studying the in-plane forces and how they evolve during rotations.

3.3 Acoustic emissions

Regarding the information on acoustic emissions, the main feature was provided by analyzing the elastic waves absolute energy evolution as a function of centroid frequencies (Fig. 8). The absolute energy is obtained by integrating over the entire burst duration the squared voltage signal [33]. The centroid frequency represents the frequency center mass of AE signals and characterizes the overall frequency content of an acoustic emission signal [34]. It can provide information about the nature of the source and help distinguish different sources of AE. In general, absolute energy has increased with the rotational speed, while the dispersion of these values and their frequency range has evolved differently depending on the alloy. For AA6082-T6, the centroid frequency is contained between 240-290 kHz for rotational speeds lower or equal to 1500 rpm. Two different features should be noted for the 2000 rpm configuration. The first is a slight shift toward lower frequencies, while the second is an increase in the dispersion of the absolute energy values. The difference in categories previously made for the tests done on AA7075-T6 can also be extended to AE analysis. Specifically, the first configuration at 500 rpm

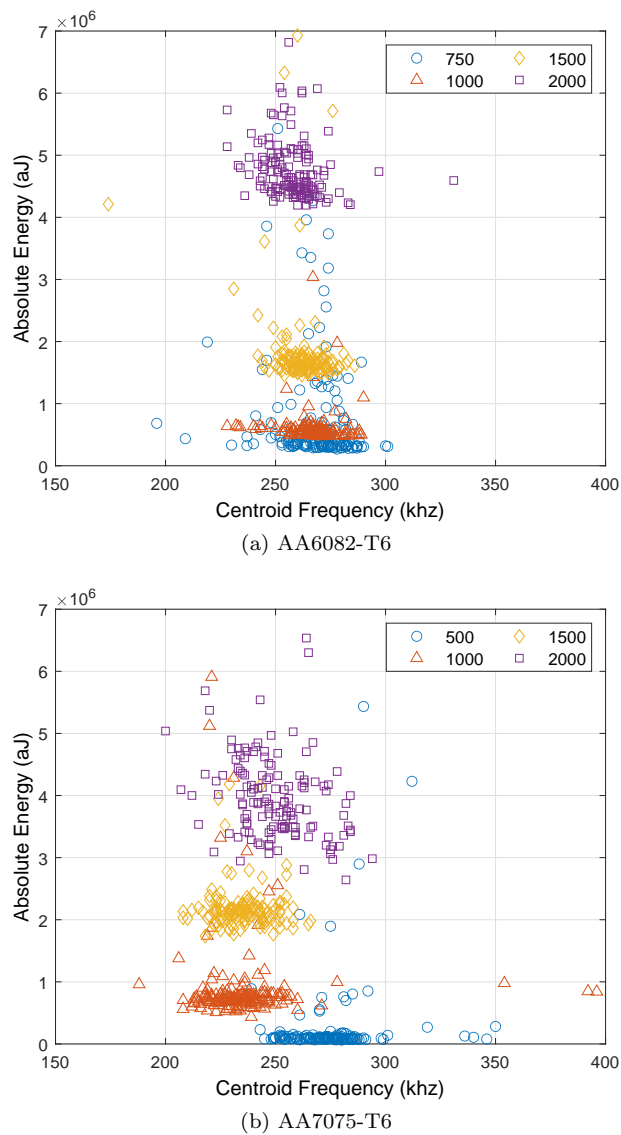


Fig. 8 Absolute energy as function of the centroid frequency for all the tests ($1aJ = 10^{-18} J$).

is distinguished from the others by the 240-290 kHz range frequencies. The intermediate configurations, 1000 and 1500 rpm are instead contained in frequencies between 210-250 kHz. The 2000 rpm configuration is different from the previous ones. Not only are the frequencies between 200 and 300 kHz, but the dispersion of the absolute energy values is significantly greater than in the other configurations. Then, regardless of the material, acoustic emission analysis allowed a division into two macro-families of joints. Those whose centroid frequency is between 240-290 kHz and the others between 210-250 kHz. This classification fits well with the observations on the periodicity of the force signals since, wherever the periodicity

turned out to be non-regular and non-coincident with a tool rotation, the centroid frequency range is 210-250 kHz, while in cases of regular evolution 240-290 kHz. Thus, the AE results corroborated the observed differences in the periodic evolution of the forces.

3.4 Welds quality

The quality of the joints was evaluated by analyzing the external surface and the cross-section. Cross-sections and details of the nugget zone (NZ) for all the AA6082-T6 friction stir welds are displayed in Fig. 9. As for the outer surface,

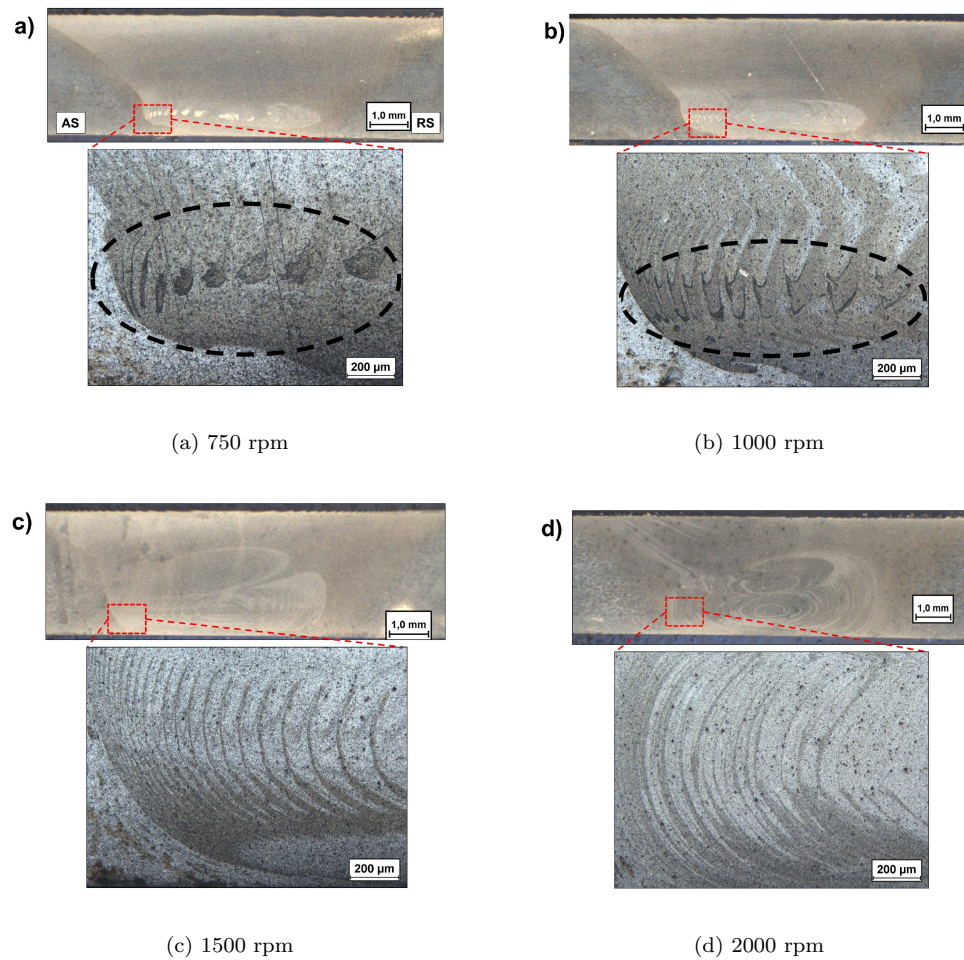


Fig. 9 Cross-sections and details of the NZ for AA6082-T6 joints.

no defects were detected. Focusing instead on the cross-sections, it is as if two

groups could be distinguished. In the first group formed by the 750 and 1000 rpm configurations, two features in Fig. 9a and b are worth noting. The first is the not distinguishable NZ with a hint of onion ring structure at the bottom of the sheet. The second highlighted in the black dashed rectangles is the micro-voids between the various packed layers constituting the onion ring in the lower part of the nugget zone on the AS that become smaller going from 750 to 1000 rpm. In the second group, 1500 and 2000 rpm, the classic onion ring structure is easily recognizable throughout NZ.

A similar analysis can be done for the AA7075-T6 joints shown in Fig. 10. The

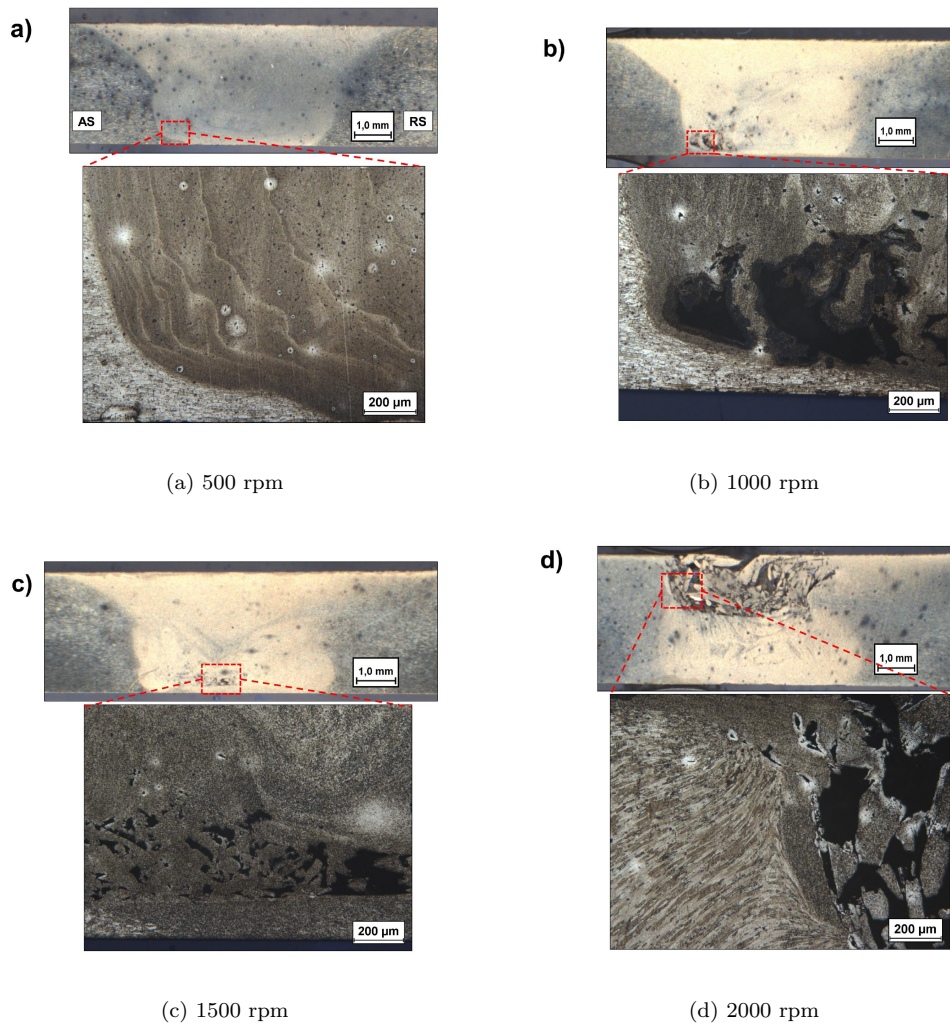


Fig. 10 Cross-sections and details of the NZ for AA7075-T6 joints.

division made earlier results evident in studying the joints' details obtained with

the different rotational speeds. The only sound joint is obtained with the lowest rotational speed, 500 rpm, as displayed in Fig. 10a. The intermediate 1000 and 1500 rpm configurations, which were characterized by the irregular period of the in-plane forces and by lower frequency range associated with the AE compared with the 500 rpm configuration, have internal defects in the NZ (Fig. 10b and c). Instead, the 2000 rpm configuration is characterized by a marked external flaw along the entire weld (Fig 11). From the cross-sectional analysis in Fig 10d, the upper central

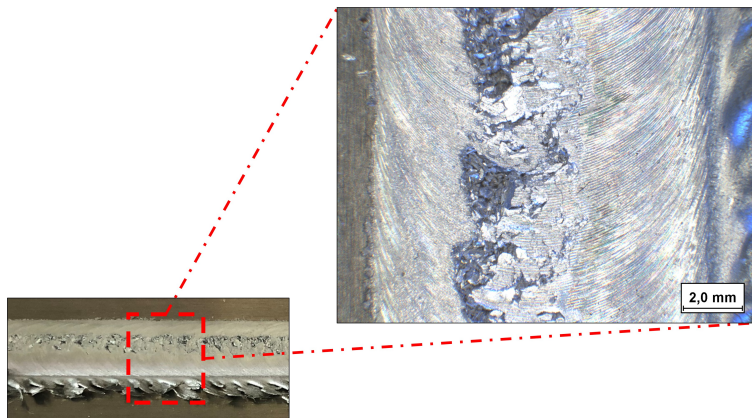


Fig. 11 External defects welding AA7075-T6 at 2000 rpm.

part of the joint is characterized by many material fragments. This macroscopic defect suggests different phenomena related to the tool-workpiece interaction and explains the marked differences observed in the monitored quantities, forces, and acoustic emissions.

The cross-section analysis showed both aluminum alloy transitions related to the material behavior during friction stir welding. For AA6082-T6, two groups were identified, 750-1000 rpm and 1500-2000 rpm, with a noticeable change in the shape and characteristics of the NZ. For AA7075-T6 alloy, on the other hand, a double transition was observed, going from sound joint (500 rpm) to internal defects (1000-1500 rpm) and then to an external defect along the entire weld seam (2000 rpm).

4 Discussion

The results presented, both quantitatively, forces and acoustic emissions, and qualitatively, joint cross-sections, provided information to infer the different plastic behavior of the two materials and the same material by changing process parameters.

The values of the welding force F_x in the various tests on the two aluminum alloys confirmed different behavior in the investigated rotational speed windows. For AA7075, the welding force is stable between 500 and 1500 rpm, as displayed in

Fig. 5. This result suggests maximum softening of the material already achieved at the lowest rotational speed [17]. Differently, the 2000 rpm configuration is characterized by an external macro defect all along the weld and by a sudden doubling of the static value of the welding force compared to the other configurations. This excessive force in the x-direction can be linked to the following phenomenon. The difficulty in shearing the volume of material while rotating determines a stronger frontal reaction since the tool rotation contribution is minimized. In other words, the incipient local melting is responsible for an increase in the slipping between tool and workpiece, and the volume of material is more pushed than sheared by the tool. In contrast, a different behavior was observed in the welding force evolution with the rotational speed for AA6082-T6 tests. Between 750 and 1500 rpm, F_x first decreases due to an increase in temperature with the rotational speed, greater thermal softening, and consequential loss in the mechanical strength of the alloy, and then stabilize between 1500 and 2000 rpm. This higher resistance of the material at rotational speeds less than or equal to 1000 rpm is also reflected in the micro-defects observed in the dashed black rectangles in Fig. 9a and b, which can be associated with the lack of mechanical bonding between the successive layers deposited successively during the advancement of the tool. Increasing the rotational speed from 750 to 1000 rpm, the size of these areas decreases, confirming a greater heat generation, mixing and bonding between the various layers, even if not yet optimal. These considerations are supported by the temperature estimation made through thermal simulation and shown in Fig. 12. For AA7075-T6, at 500 rpm, the

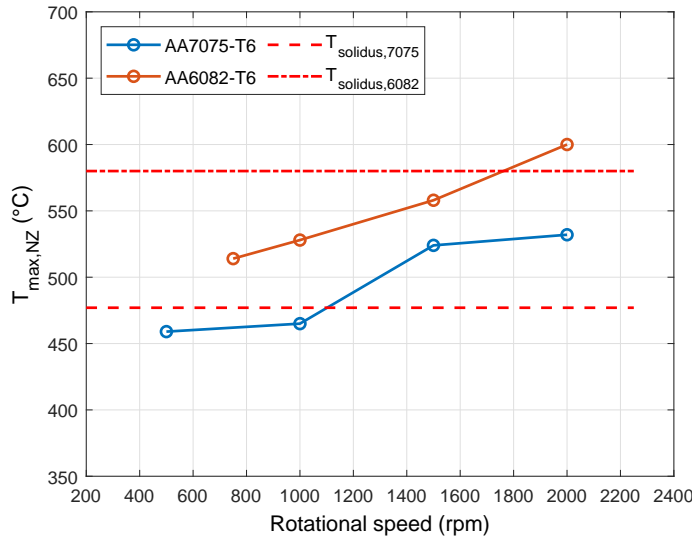
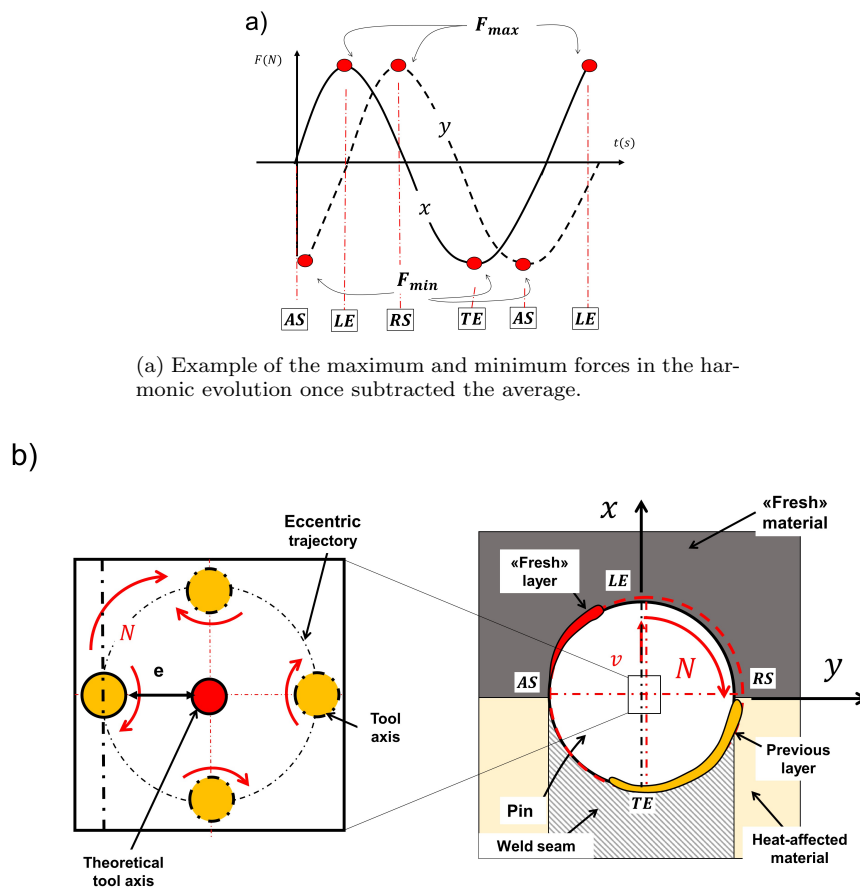


Fig. 12 Maximum temperature in the NZ for both materials in all the tested configurations.

temperature is already close to the solidus temperature, and the material softening had already reached its natural limit. The further increase of the rotational speed is responsible for a higher shear rate and increased risk of local incipient melting. On the contrary, concerning AA6082-T6, the configurations at 750 and 1000 rpm, the temperature is still far enough from the solidus. By increasing the rotational

speed, there is a greater softening of the material with consequent reduction of the resistance offered by the latter. Hence, the relatively cold first welds (i.e., 750 and 1000 rpm) with the unusual appearance of onion rings only in the lower part of NZ and the micro-defects between the various layers resulting from an incorrect stirring were confirmed. These results are coherent with the thermal properties of the aluminum alloys. For AA7075, the maximum softening can be reached for low rotational speed being characterized by lower T_s and thermal conductivity compared to AA6082. Consequently, the higher rotational speed can easily induce local incipient melting in the hottest point during friction stir welding, i.e., the corner between pin and shoulder [35], impeding the correct plastic deformation of the material layer around the tool increasing the reaction in the welding direction. On the other hand, the relatively cold welds obtained with the lowest rotational speed for AA6082 are coherent with their thermal properties. Higher heat generation is required to increase the temperature in the material due to the higher thermal conductivity (i.e., faster heat dissipation). It is also interesting to observe the relation between F_x and F_y in all the tested configurations. When sufficient heat input for the correct softening and stirring of the material was guaranteed, $F_y > F_x$. On the other hand, for the relatively cold welds, 750 and 1000 rpm for AA6082 (Fig. 9a and b), $F_x > F_y$. Therefore, this relationship can be an indicator of understanding whether the chosen welding configurations guarantee the achievement of temperatures close to the solidus temperature or not. This analysis excluded the configuration at 2000 rpm on AA7075 not comparable with the others because of the external macro-defects.

To understand the observed differences in the periodicity of force signals, it is necessary to focus locally on single rotations. The average value was subtracted from the forces to analyse only the harmonic part of the signals, and the cyclical peaks (F_{max}) and valleys (F_{min}) were highlighted (Fig. 13a). In-plane forces oscillation is associated with the eccentricity of the process [36] introduced by the system, the tool, and the interaction with the material to be welded [37]. Hence, during its period, the tool is making two different movement associates with the rotation. It rotates around its axis due to the spindle action. Simultaneously, its axis revolves around the theoretical tool axis. The two movements are displayed in the sketch in Fig. 13b. The eccentric motion is responsible for the reactions with the material around the pin, and the force sensor sees with a 90° offset the same thing along x and y (Fig. 14). However, due to the tool's rotation around its axis, a second pin-workpiece interaction also intervenes. The tool shears a portion of the material because of its rotation. Under optimal welding conditions, the material layer is deformed and sheared around the tool following its eccentric revolution. Therefore, the pin radius at the eccentric side increases due to the sheared material layer, further increasing the compression exerted on the matrix around the pin, generating the in-plane forces oscillation, as displayed in Fig. 13a. The interaction with the material layer ends during the eccentric rotation towards the trailing edge (TE), where space is created due to the tool advancing, and then the layer is released and compressed against the previously deposited layer. The consequences of the tool axis's rotation and revolution are the cyclical processing of successive layers and the cyclical increase/decrease of the forces. To associate the peaks of the two forces with a specific tool position in proper stirring condition, the following assumption is made. When the tool is in the eccentric position towards the leading edge (LE), the y component is zero while the one along x is maximum (Fig. 14b).



(a) Example of the maximum and minimum forces in the harmonic evolution once subtracted the average.

(b) Focus on the eccentricity. Tool rotation around itself (i.e. around the tool axis) and revolution around the theoretical tool axis (i.e. rotation of the tool axis around the theoretical tool axis).

Fig. 13 Explanation of the link between forces oscillation and tool revolution. a) In-plane forces oscillation, b) tool axis rotation and revolution in one period.

When after 90° the tool is towards RS, the x component is zero, while F_y reaches its maximum, as displayed in Fig. 14c. The same, but in the opposite direction, happens on the TE and AS. To summarize everything, $F_{x,max}$ in LE, $F_{y,max}$ in RS, $F_{x,min}$ in TE, and $F_{y,min}$ in AS according to the orientation of the loadcell, welding direction and rotation. The resultant is equal to F_x or F_y in the conditions shown in Fig. 14, while it is composed of an x and y component in all others. Similarly, the resultant angle with the welding direction (clockwise direction) can also be calculated. In Fig. 15, the evolution of the in-plane forces, the resultant and its angle (α) with respect to the welding direction during three rotations in the AA6082-T6 configuration at 1500 rpm are shown. In-plane forces evolve regularly with a periodicity equal to the tool rotation with one peak and one valley. The

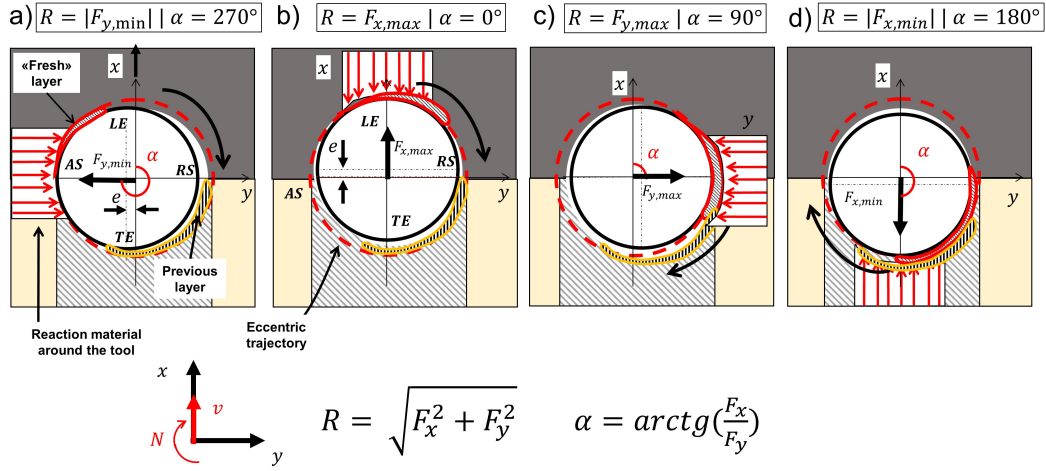


Fig. 14 Tool revolution during the rotation each 90° . a) AS, b) LE, 3) RS, 4) TE.

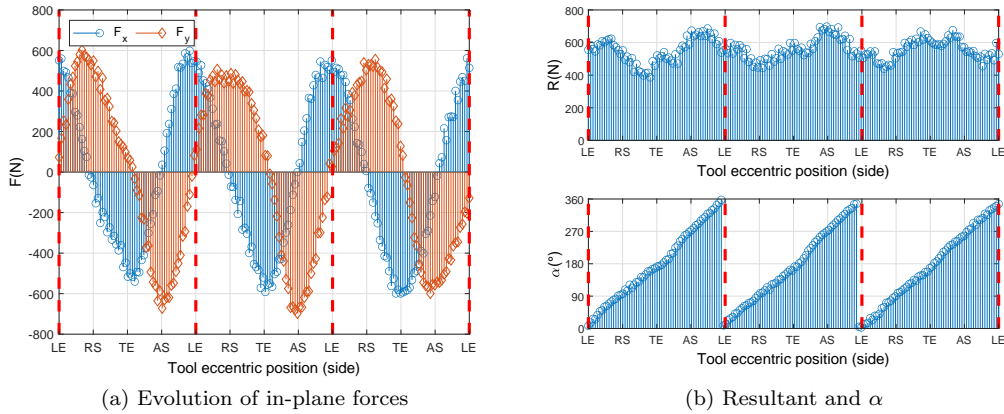


Fig. 15 Focus on three rotations while welding AA6082-T6 at 1500 rpm.

resultant angle varies between 0° and 360° in one rotation following the eccentric trajectory of the tool, and its value oscillates between 400 and 700 N. Contrarily, for AA7075, in the 1000 rpm configuration (Fig. 16), in-plane forces evolve irregularly without the expected periodicity equal to the tool rotation. The resultant angle with the welding direction does not complete the 360° in one tool rotation, and its value oscillates between 50 and 800 N (Fig. 16b). The critical element is the unexpected difference between peaks F_x and F_y in the second rotation (black dashed rectangle in Fig. 16a). Throughout the weld, in AA6082 considered configuration, the F_x and F_y peaks are always very similar. On the contrary, in the case

of AA7075, this marked difference cyclically occurs. If the interaction between the coupled pin-layer and the base material around the pin is considered equal during the rotation, the values of the two forces should not differ much. Hence, the sudden y-force drop is explained by material failure during the plastic deformation (i.e. compression due to the revolution and shearing due to the rotation).

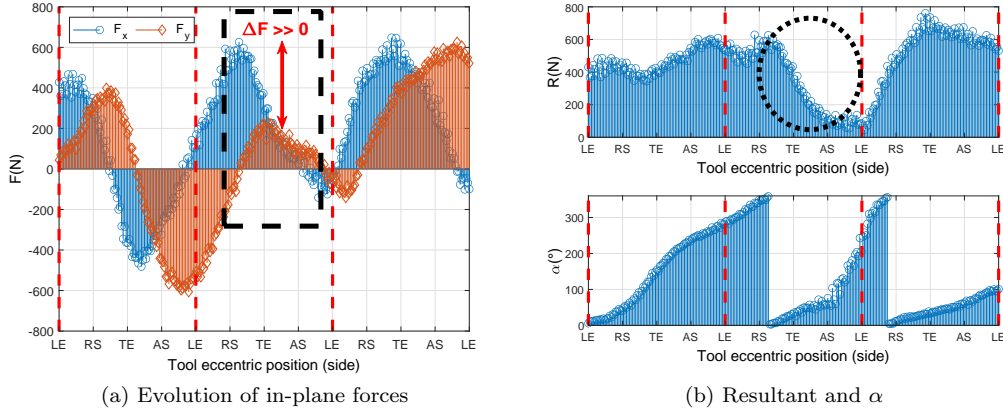


Fig. 16 Focus on three rotations while welding AA7075-T6 at 1000 rpm.

The fractures determine a de-phasing between the revolution and the sheared layer position around the tool, causing instabilities in the forces. This phenomenon can also be analyzed by observing the in-plane forces' evolution during one revolution when displayed in the compass plot, Fig. 17 and Fig. 18, focusing on the second rotation of Fig. 15 and Fig. 16, respectively. Under stable conditions, the resultant is always directed toward the eccentric position of the tool (Fig. 17), whereas this effect is lost under unstable welding conditions (Fig. 18). This phenomenon may result from a fragmented plastic deformation of the material layer rather than continuous, giving rise to irregularities in the force signals and defects within the weld bead.

In FSW, the increase in rotational speed keeping constant the welding speed determines APR decreases (the volume processed per rotation) and the greater local concentration of stress and plastic deformation in a smaller portion of material. Regarding AA7075-T6, the maximum temperatures shown in Fig. 12 reached at 500 rpm is very close to the solidus temperature. Thus, the increase in rotational speed combined with a higher concentration of plastic deformation induces a local temperature increase exceeding the solidus temperature, causing instability in the process. Similar findings have been found when investigating the hot extrusion of aluminum alloys. Studying the deformability of various aluminum alloys, Zakharov [38] demonstrated the significant difference between AA7075 and AA6xxx during hot extrusion. The low deformability of AA7075 is due to its sensitivity to hot tearing defect [39]. This defect consists of micro-cracks on the external surface of the extrudates (Fig. 19) due to high temperatures close to or above the solidus

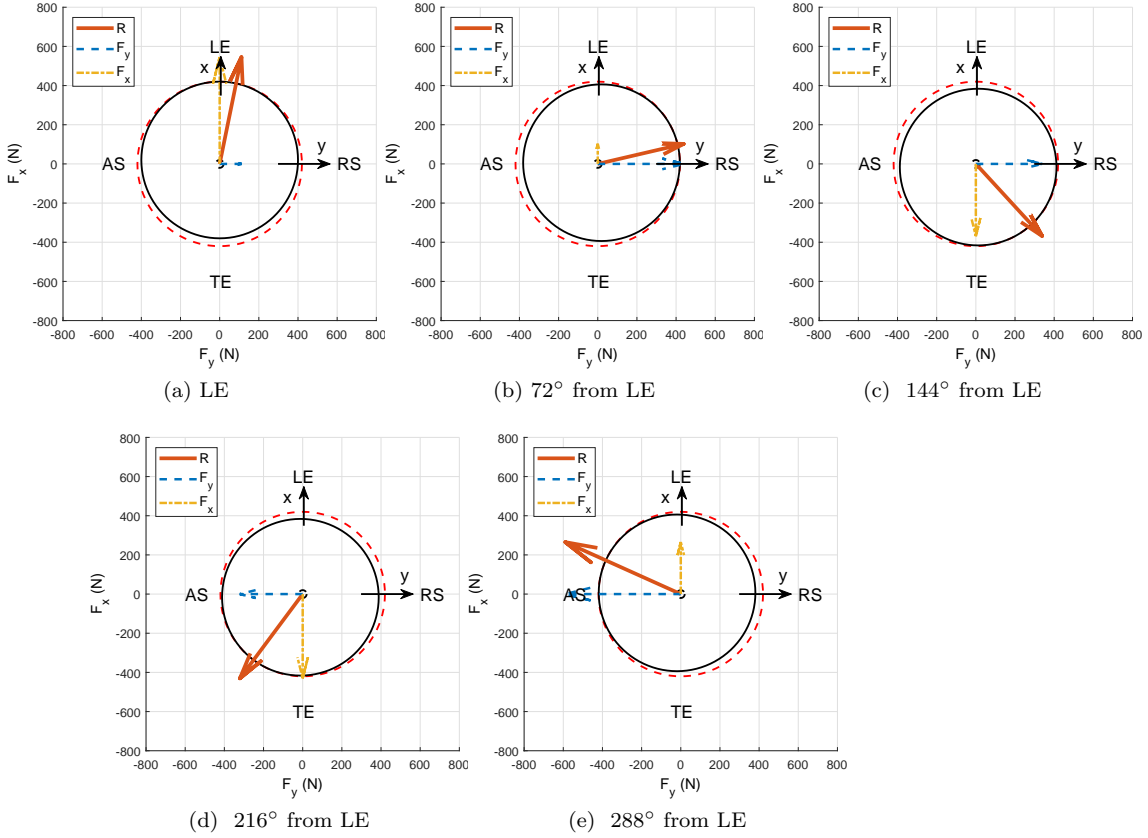


Fig. 17 In-plane forces evolution in one tool revolution while welding AA6082-T6 at 1500 rpm. The eccentric position is indicated below each picture with respect to the LE.

temperature reached in correspondence of the stress concentration zones at the die edges.

The increase in temperature above the solidus temperature is responsible for local incipient melting in second phase particles causing sudden embrittlement of the material with its resistance dropping below the flow stress previously required for the plastic deformation. The consequence is the unexpected fracture with the appearance of tears on the external surface of the extruded part [41]. This defect is more likely to appear in heavily alloyed aluminum, characterized by the high density of intragranular and intergranular second phase particles [42]. For the same reason, in FSW of heavily alloyed aluminum such as AA7075-T6, the rotational speed represents a critical parameter for the occurrence of a phenomenon similar to hot tearing in extrusion, here defined as intermittent material flow. The intermittent material flow is likely responsible for the occurrence of flow defects during the process. A sketch to compare continuous and intermittent material flow is shown in Fig. 20. Between Step2 and Step4, the plastic deformation concentration due to compression and shear action performed by the tool on the small volume of material can lead to local fracture of the layer processed by the tool.

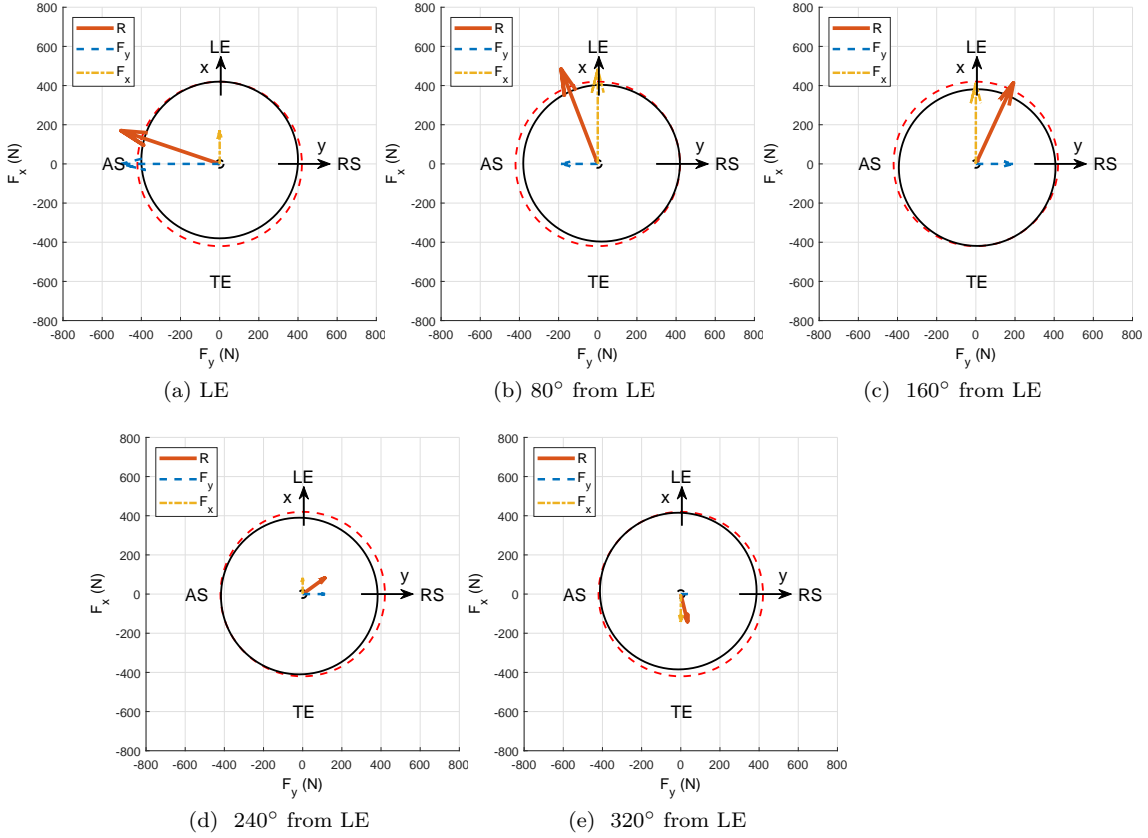


Fig. 18 In-plane forces evolution in one tool revolution while welding AA7075-T6 at 1000 rpm. The eccentric position is indicated below each picture respect to the LE.

The point at which this phenomenon occurs depends not only on the thermo-mechanical conditions but also on the material's microstructure, i.e. second phase particles density. Hence, to guarantee continuous material flow, it is necessary to choose the appropriate rotational speed according to the material, welding speed, axial force or plunge depth, clamping system, backing plate, and tool. If the critical rotational speed is exceeded, the intermittent material flow may occur. This critical value is lower for materials characterized by low deformability, and consequently, they have a narrower weldability window. This phenomenology explains the connection between high rotational speeds and internal voids previously referred to as abnormal stirring [43].

Acoustic emissions corroborate the introduced concept of continuous and intermittent material flow. As displayed in Fig. 8 the conditions characterized by the intermittent material flow, 1000 and 1500 rpm welding AA7075-T6, presented a different range of frequencies associated with the absolute energy of the acoustic emission compared to the others. The shifted elastic wave frequencies confirm a different nature of the source of these emissions, justifying the intermittent material flow. In conclusion, AE reinforced the concept of intermittent flow when

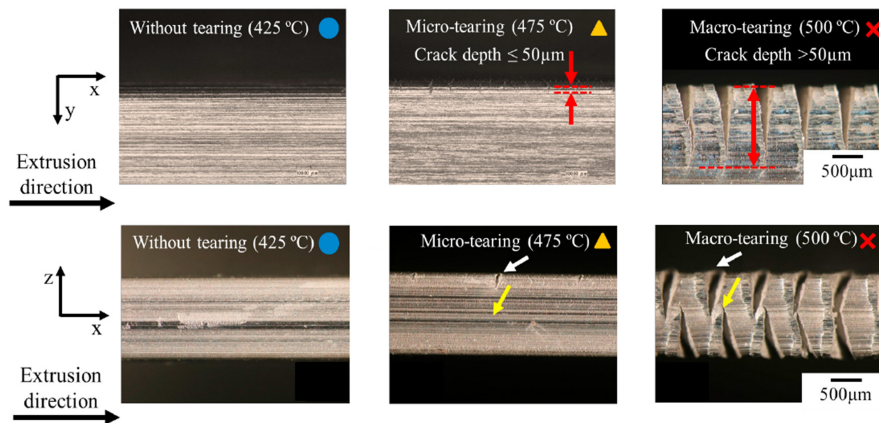


Fig. 19 Hot tearing in AA7075 hot extrusion [40].

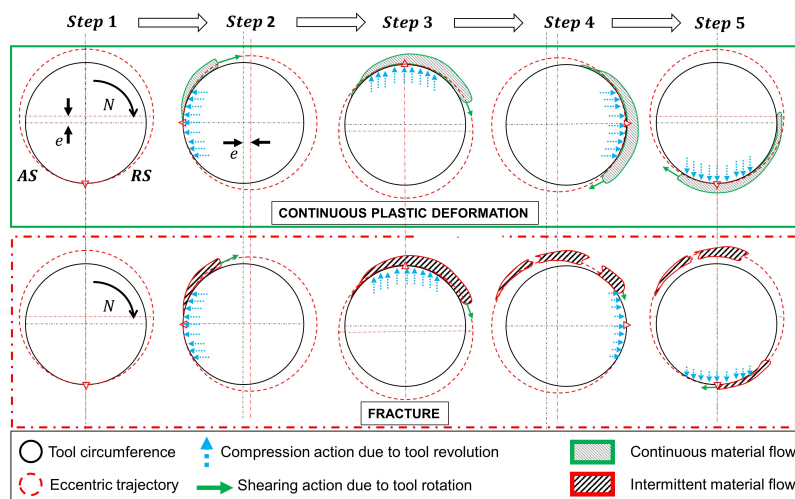
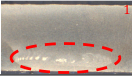
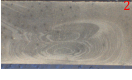
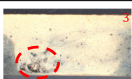
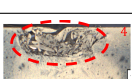


Fig. 20 Differences between continuous and intermittent material flow.

the maximum temperature in NZ is attained and too high rotational speed are employed.

In Tab. 3, all the differences observed in the various tests are summarized with a division into groups according to the characteristics observed in the in-plane forces, acoustic emissions, weld quality, and type of material flow. Acoustic emissions in the centroid frequency range between 210 and 250 kHz and forces period equal to the tool rotation period correspond to a continuous material flow, group 1 and 2. However, the difference between the two groups was inferred from the relationship between the mean value of F_x and F_y and the quality of the joints. To group 1 belong cold joints, in thermal conditions still not optimal and $F_x > F_y$, while to

Table 3 Summary of the experimental results. Base material (BM), weld quality (WQ), material flow (MF). Continuous (C) and Intermittent (I).

Group	BM	N (rpm)	Mean	Period	AE (kHz)	WQ	MF
1	6082	750	$F_x > F_y$	~ 1 rot	240-290		C
		1000					
2	6082	1500	$F_x < F_y$	~ 1 rot	240-290		C
		2000					
3	7075	500	$F_x < F_y$	> 1 rot	210-250		I
		1000					
4	7075	1500	$F_x < F_y$	> 1 rot	210-250		I
		2000					

group 2 the necessary thermal conditions (between $0.9 T_s < T_{max,NZ} < 1.05 T_s$) to guarantee a correct stirring of the material had occurred and $F_x < F_y$. The joints of group 3 are characterized by the forces period not equal to a tool rotation period and by a range of centroid frequencies different from the previous one. In qualitative terms, it resulted in the presence of internal voids. Thanks to the local analysis of single rotations, the outcome was explained by an intermittent material flow justifying both the difference in the monitored physical quantities (forces and AE) and the presence of the defects. Finally, the only joint belonging to group 4 represents an extreme condition of intermittent material flow. The severe thermomechanical conditions (the high temperature and shear rate) led to incipient local melting with the consequent slipping between pin and layer, giving rise to this macroscopic external defect. In terms of physical quantities monitored, this leads to an F_x almost twice F_y and a range of centroid frequencies extending over continuous and intermittent domains.

5 Conclusion

In the present investigation, the plastic behavior of AA6082-T6 and AA7075-T6 was investigated by friction stir welding using the same welding parameters and monitoring in-plane forces and acoustic emission.

The first highlight is the different rotational speed range to guarantee the maximum softening and, consequently, the maximum attainable temperatures because of the friction between tool and material. For AA6082-T6, the stability of the in-plane static forces components is obtained between 1500 and 2000 rpm, while AA7075-T6 between 500 and 1500 rpm with maximum softening conditions already obtained at 500 rpm. This is justified by the different thermal characteristics of the two alloys with AA7075-T6 having a lower thermal conductivity facilitating the local increase in temperature approaching the solidus.

Using too high rotational speeds can result in an intermittent material flow instead of a continuous one. An intermittent material flow generates possible voids inside

the joint due to incorrect material stirring. This phenomenon may appear if the following conditions occur:

- The maximum temperature in the NZ has already reached the solidus one, and the rotational speed is further increased.
- The volume of material processed, dependent on thickness and APR, is reduced, resulting in a significant concentration of plastic deformation in a small amount of material.

In the presence of these two conditions, the critical rotational speed is significantly reduced if the alloy is characterized by a high percentage of alloying elements and consequently a high density of second phase particles. This conclusion was based on the plastic deformation localization in the sheared material volume combined with the irregularities in the force signals' dynamic part, which suggested the failure during plastic deformation. The hypothesis made on the possible different material flows depending on friction stir welding conditions was then corroborated by the difference in the acoustic emissions characteristics depending on the type of configuration, continuous or intermittent flow. Given these results, the different plastic behavior of the two materials due to their microstructure is evident. The higher deformability and consequent lower sensitivity to the intermittent material flow of AA6082-T6 determines a wider weldability window. Contrarily, for AA7075-T6, more attention is required to avoid intermittent material flow and possible internal defects by choosing the appropriate rotational speed.

Declarations

Funding

This project received funding from the European Union's Marie Skłodowska-Curie Actions (MSCA) Innovative Training Networks (ITN) H2020-MSCA-ITN-2017 under the grant agreement N°764979.

Contributions

Danilo Ambrosio: Conceptualization, Methodology, Formal analysis, Investigation, Data Curation, Writing - Original Draft, Writing - Review and Editing, Visualization. **Vincent Wagner:** Conceptualization, Methodology, Formal analysis, Writing - Review and Editing. **Gilles Dessein:** Conceptualization, Methodology, Formal analysis, Investigation, Writing - Review and Editing, Supervision, Project administration. **Jean-Yves Paris:** Writing - Review and Editing. **Kholoud Jlaiel:** Writing - Review and Editing. **Olivier Cahuc:** Writing - Review and Editing, Supervision, Project administration, Funding acquisition.

Ethics approval

Not applicable

Consent to participate

I am agreeing to participate.

Consent for publication

I am agreeing to publish this work.

Conflict of interest

The authors declare no competing interests.

References

1. W.M. Thomas, E.D. Nicholas, J.C. Needham, M.G. Murch, P. Templesmith, C.J. Dawes (1995) U.S. Patent No. 5,460,317, October 24
2. Engler, O., Hirsch, J. (2002). Texture control by thermomechanical processing of AA6xxx Al-Mg-Si sheet alloys for automotive applications - a review. *Materials Science and Engineering A*, 336(1-2), 249262. [https://doi.org/10.1016/S0921-5093\(01\)01968-2](https://doi.org/10.1016/S0921-5093(01)01968-2)
3. Ribeiro, F. C., Scarpin, B. T., Batalha, G. F. (2016). Experimental and numerical modelling and simulation of the creep age forming of aeronautic panels AA7XXX aluminium alloy. *Advances in Materials and Processing Technologies*, 2(1), 1-20. <https://doi.org/10.1080/2374068X.2016.1147764>
4. Cavaliere, P., Squillace, A., Panella, F. (2008). Effect of welding parameters on mechanical and microstructural properties of AA6082 joints produced by friction stir welding. *Journal of Materials Processing Technology*, 200(1-3), 364-372. <https://doi.org/10.1016/j.jmatprotec.2007.09.050>
5. Leitão, C., Louro, R., Rodrigues, D. M. (2012). Analysis of high temperature plastic behaviour and its relation with weldability in friction stir welding for aluminium alloys AA5083-H111 and AA6082-T6. *Materials and Design*, 37, 402-409. <https://doi.org/10.1016/j.matdes.2012.01.031>
6. Ramulu, P. J., Narayanan, R. G., Kailas, S. V., Reddy, J. (2013). Internal defect and process parameter analysis during friction stir welding of Al 6061 sheets. *International Journal of Advanced Manufacturing Technology*, 65(9-12), 1515-1528. <https://doi.org/10.1007/s00170-012-4276-z>
7. Forcellese, A., Simoncini, M., Casalino, G. (2017). Influence of process parameters on the vertical forces generated during friction stir welding of AA6082-T6 and on the mechanical properties of the joints. *Metals*, 7(9), 1-13. <https://doi.org/10.3390/met7090350>
8. Lambiase, F., Paoletti, A., Di Ilio, A. (2018). Forces and temperature variation during friction stir welding of aluminum alloy AA6082-T6. *International Journal of Advanced Manufacturing Technology*, 99(1-4), 337-346. <https://doi.org/10.1007/s00170-018-2524-6>
9. Azimzadegan, T., Serajzadeh, S. (2010). An investigation into microstructures and mechanical properties of AA7075-T6 during friction stir welding at relatively high rotational speeds. *Journal of Materials Engineering and Performance*, 19(9), 1256-1263. <https://doi.org/10.1007/s11665-010-9625-1>
10. Bahemmat, P., Besharati, M. K., Haghpanahi, M., Rahbari, A., Salekrostam, R. (2010). Mechanical, micro-, and macrostructural analysis of AA7075-T6 fabricated by friction stir butt welding with different rotational speeds and tool pin profiles. *Proceedings of the Institution of Mechanical Engineers, Part B: Journal of Engineering Manufacture*, 224(3), 419-433. <https://doi.org/10.1243/09544054JEM1554>
11. Gemme, F., Verreman, Y., Dubourg, L., Wanjara, P. (2011). Effect of welding parameters on microstructure and mechanical properties of AA7075-T6 friction stir welded joints (pp. 877-886). pp. 877-886. <https://doi.org/10.1111/j.1460-2695.2011.01580.x>
12. Rajakumar, S., Muralidharan, C., Balasubramanian, V. (2011). Influence of friction stir welding process and tool parameters on strength properties of AA7075-T6 aluminium alloy joints. *Materials and Design*, 32(2), 535-549. <https://doi.org/10.1016/j.matdes.2010.08.025>
13. Ipekolu, G., Kiral, B. G., Erim, S., am, G. (2012). Investigation of the effect of temper condition on the friction-stir weldability of AA7075 Al-alloy plates. *Materiali in Tehnologije*, 46(6), 627632.
14. Zhang, C., Huang, G., Cao, Y., Zhu, Y., Liu, Q. (2019). On the microstructure and mechanical properties of similar and dissimilar AA7075 and AA2024 friction stir welding joints: Effect of rotational speed. *Journal of Manufacturing Processes*, 37(December 2018), 470-487. <https://doi.org/10.1016/j.jmapro.2018.12.014>
15. Ambrosio, D., Wagner, V., Garnier, C., Jacquin, D., Tongne, A., Fazzini, M., Dessein, G. (2020). Influence of welding parameters on the microstructure, thermal fields and defect formation in AA7075-T6 friction stir welds. *Welding in the World*, 64(5), 773-784. <https://doi.org/10.1007/s40194-020-00869-4>
16. Ambrosio, D., Garnier, C., Wagner, V., Aldanondo, E., Dessein, G., Cahuc, O. (2020). Relationships between welding parameters, aging conditions, and weld properties in AA7075-T6 friction stir welds. *International Journal of Advanced Manufacturing Technology*, 111(5-6), 1333-1350. <https://doi.org/10.1007/s00170-020-06184-y>
17. Long, T., Tang, W., Reynolds, A. P. (2007). Process response parameter relationships in aluminium alloy friction stir welds. *Science and Technology of Welding and Joining*, 12(4), 311-317. <https://doi.org/10.1179/174329307X197566>

18. Astarita, A., Squillace, A., Carrino, L. (2014). Experimental Study of the Forces Acting on the Tool in the Friction-Stir Welding of AA 2024 T3 Sheets. *Journal of Materials Engineering and Performance*, 23(10), 3754-3761. <https://doi.org/10.1007/s11665-014-1140-3>
19. Doude, H., Schneider, J., Patton, B., Stafford, S., Waters, T., Varner, C. (2015). Optimizing weld quality of a friction stir welded aluminum alloy. *Journal of Materials Processing Technology*, 222, 188-196. <https://doi.org/10.1016/j.jmatprotec.2015.01.019>
20. Shrivastava, A., Zinn, M., Duffie, N. A., Ferrier, N. J., Smith, C. B., Pfefferkorn, F. E. (2017). Force measurement-based discontinuity detection during friction stir welding. *Journal of Manufacturing Processes*, 26, 113-121. <https://doi.org/10.1016/j.jmapro.2017.01.007>
21. Franke, D., Rudraraju, S., Zinn, M., Pfefferkorn, F. E. (2020). Understanding process force transients with application towards defect detection during friction stir welding of aluminum alloys. *Journal of Manufacturing Processes*, 54(November 2019), 251-261. <https://doi.org/10.1016/j.jmapro.2020.03.003>
22. Chen, C., Kovacevic, R., Jandgric, D. (2003). Wavelet transform analysis of acoustic emission in monitoring friction stir welding of 6061 aluminum. *International Journal of Machine Tools and Manufacture*, 43(13), 1383-1390. [https://doi.org/10.1016/S0890-6955\(03\)00130-5](https://doi.org/10.1016/S0890-6955(03)00130-5)
23. Soundararajan, V., Atharifar, H., Kovacevic, R. (2006). Monitoring and processing the acoustic emission signals from the friction-stir-welding process. *Proceedings of the Institution of Mechanical Engineers, Part B: Journal of Engineering Manufacture*, 220(10), 1673-1685. <https://doi.org/10.1243/09544054JEM586>
24. Rajashekar, R., Rajaprakash, B. M. (2016). Development of a model for friction stir weld quality assessment using machine vision and acoustic emission techniques. *Journal of Materials Processing Technology*, 229, 265-274. <https://doi.org/10.1016/j.jmatprotec.2015.09.030>
25. *Metals Handbook, Vol.2 - Properties and Selection: Nonferrous Alloys and Special-Purpose Materials*, ASM International 10th Ed. 1990.
26. Wang, P. L., Jiang, H. T., Zhang, R. J., Huang, S. Y. (2016). Study of Hot Deformation Behavior of 6082 Aluminum Alloy. *Materials Science Forum*, 877, 340-346. <https://doi.org/10.4028/www.scientific.net/msf.877.340>
27. Cadoni, E., Dotta, M., Forni, D., Kaufmann, H. (2016). Effects of strain rate on mechanical properties in tension of a commercial aluminium alloy used in armour applications. *Procedia Structural Integrity*, 2, 986-993. <https://doi.org/10.1016/j.prostr.2016.06.126>
28. Ulysse, P. (2002). Three-dimensional modeling of the friction stir-welding process. *International Journal of Machine Tools and Manufacture*, 42(14), 1549-1557. [https://doi.org/10.1016/S0890-6955\(02\)00114-1](https://doi.org/10.1016/S0890-6955(02)00114-1)
29. Mijajlovi, M. M., Pavlovi, N. T., Jovanovi, S. V., Jovanovi, D. S., Mili, M. D. (2013). Experimental studies of parameters affecting the heat generation in friction stir welding process. *Thermal Science*, 16(SUPPL.2), 351-362. <https://doi.org/10.2298/TSCI120430174M>
30. Schmidt, H., Hattel, J., Wert, J. (2004). An analytical model for the heat generation in friction stir welding. *Modelling and Simulation in Materials Science and Engineering*, 12(1), 143157. <https://doi.org/10.1088/0965-0393/12/1/013>
31. Khandkar, M. Z. H., Khan, J. A., Reynolds, A. P. (2003). Prediction of temperature distribution and thermal history during friction stir welding : input torque based model. *Science and Technology of Welding and Joining*, (June). <https://doi.org/10.1179/136217103225010943>
32. Fehrenbacher, A., Duffie, N. A., Ferrier, N. J., Pfefferkorn, F. E., Zinn, M. R. (2014). Effects of tool-workpiece interface temperature on weld quality and quality improvements through temperature control in friction stir welding. *International Journal of Advanced Manufacturing Technology*, 71(1-4), 165-179. <https://doi.org/10.1007/s00170-013-5364-4>
33. Jlaiel, K., Yahiaoui, M., Paris, J. Y., Denape, J. (2020). Tribolumen: A tribometer for a correlation between ae signals and observation of tribological process in real-time-application to a dry steel/glass reciprocating sliding contact. *Lubricants*, 8(4). <https://doi.org/10.3390/LUBRICANTS8040047>
34. Yahiaoui, M., Chabert, F., Paris, J. Y., Nassiet, V., Denape, J. (2019). Friction, acoustic emission, and wear mechanisms of a PEKK polymer. *Tribology International*, 132, 154164. <https://doi.org/10.1016/j.triboint.2018.12.020>
35. Silva-Magalhes, A., De Backer, J., Martin, J., Bolmsj, G. (2019). In-situ temperature measurement in friction stir welding of thick section aluminium alloys. *Journal of Manufacturing Processes*, 39(February), 12-17. <https://doi.org/10.1016/j.jmapro.2019.02.001>

36. Yan, J. H., Sutton, M. A., Reynolds, A. P. (2007). Processing and banding in AA2524 and AA2024 friction stir welding. *Science and Technology of Welding and Joining*, 12(5), 390-401. <https://doi.org/10.1179/174329307X213639>
37. Shah, L. H., Walbridge, S., Gerlich, A. (2019). Tool eccentricity in friction stir welding: A comprehensive review. *Science and Technology of Welding and Joining*, 24(6), 566578. <https://doi.org/10.1080/13621718.2019.1573010>
38. Zakharov, V. V. (1995). Scientific aspects of deformability of aluminum alloys during extrusion. *Advanced Performance Materials*, 2(1), 5165. <https://doi.org/10.1007/BF00711651>
39. Reza, A., Zhou, J., Duszczak, J. (2011). Microstructural Evolution During the Homogenization of Al-Zn-Mg Aluminum Alloys. *Recent Trends in Processing and Degradation of Aluminium Alloys*, (March 2015). <https://doi.org/10.5772/34695>
40. Ngernbamrung, S., Suzuki, Y., Takatsuji, N., Dohda, K. (2018). Investigation of surface cracking of hot-extruded AA7075 billet. *Procedia Manufacturing*, 15, 217224. <https://doi.org/10.1016/j.promfg.2018.07.212>
41. Sigworth, G. K. (1996). Hot Tearing of Metals. *AFS Transactions-American Foundry*, 10531062. Retrieved from papers3://publication/uuid/85386CF4-29C7-4099-94CA-3244BD680230
42. Stoloff, N. S. (1983). Liquid and solid metal embrittlement. *Atomics of fracture*, 921-947.
43. Kim, Y. G., Fujii, H., Tsumura, T., Komazaki, T., Nakata, K. (2006). Three defect types in friction stir welding of aluminum die casting alloy. *Materials Science and Engineering A*, 415(1-2), 250-254. <https://doi.org/10.1016/j.msea.2005.09.072>